

MEASURING THE REDSHIFT DEPENDENCE OF THE CMB MONOPOLE TEMPERATURE WITH PLANCK DATA.

I. DE MARTINO¹, F. ATRIO-BARANDELA¹, A. DA SILVA², H. EBELING³, A. KASHLINSKY⁴, D. KOCEVSKI⁵, C.J.A.P. MARTINS²

Draft version February 25, 2013

ABSTRACT

We study the power of PLANCK data to constrain deviations of the Cosmic Microwave Background black body temperature from adiabatic evolution using the thermal Sunyaev-Zeldovich anisotropy induced by clusters of galaxies. We consider two types of data sets: the cosmological signal is removed in the Time Ordered Information or is removed from the final maps; and two different statistical estimators, based on the ratio of temperature anisotropies at two different frequencies and on a fit to the spectral variation of the cluster signal with frequency. To test for systematics, we construct a template from clusters drawn from a hydro-simulation included in the pre-launch Planck Sky Model. We demonstrate that, using a proprietary catalog of X-ray selected clusters with measured redshifts, electron densities and X-ray temperatures, we can constrain deviations of adiabatic evolution, measured by the parameter α in the redshift scaling $T(z) = T_0(1+z)^{1-\alpha}$, with an accuracy of $\sigma_\alpha = 0.011$ in the most optimal case and with $\sigma_\alpha = 0.016$ for a less optimal case. These results represent a factor 2-3 improvement over similar measurements carried out using quasar spectral lines and a factor 6-20 with respect to earlier results using smaller cluster samples.

Subject headings: Cosmic Microwave Background. Cosmology: theory. Cosmology: observations

1. INTRODUCTION

One of the fundamental tenets of the Big-Bang paradigm is the adiabatic evolution of the Universe. Early thermal equilibrium among the different particle species, entropy and photon number conservation produce a Cosmic Microwave Background (CMB) with a blackbody spectrum. The CMB temperature was measured to be $T_0 = 2.725 \pm 0.002$ K by the Far Infrared Absolute Spectrometer (FIRAS) of the Cosmic Background Explorer (COBE) satellite (Mather et al 1999). The adiabatic expansion of the Universe and photon number conservation imply that the CMB temperature evolves with redshift as $T(z) = T_0(1+z)$. Establishing observationally this relation would test our current understanding of the Universe since models like decaying vacuum energy density and gravitational ‘adiabatic’ photon creation predict different scaling relations (Overduin & Cooperstock, 1998; Matyjasek 1995; Lima et al 2000; Puy 2004; Jetzer et al 2011, Jetzer & Tortora 2012). In these models, energy is slowly injected without producing distortions on the blackbody spectrum, evading the tight FIRAS constraints. Nevertheless, in these models the blackbody temperature scales nonlinearly as $T(z) = T_0(1+z)^{1-\alpha}$. Therefore, measuring the redshift dependence of the CMB black body temperature at various cosmological epochs can provide strong constraints on physical theories at the fundamental level.

There are currently two methods to determine $T(z)$ at redshifts $z > 0$: (a) using fine structure lines from interstellar atoms or molecules, present in quasar spectra, whose transition energies are excited by the CMB photon bath (Bahcall & Wolfe, 1968) and (b) from the thermal Sunyaev-Zeldovich anisotropies (hereafter TSZ, Sunyaev & Zel’dovich, 1972, 1980) due to the inverse Compton scattering of photons by the free electrons within the potential wells of clusters of galaxies. Early observations of fine-structure levels of atomic species like carbon only led to upper limits on $T(z)$ because the CMB is not the only radiation field populating the energy levels and collisional excitation is an important contribution. Assuming the CMB is the only source of excitation, Songaila et al. (1994) measured $T(z = 1.776) = 7.4 \pm 0.8$ K; but collisional excitation was not negligible and it had to be corrected. The first unambiguous measurement was only achieved six years later, with a considerably larger error bar (Srianand et al. 2000). Lately, Noterdaeme et al (2010) succeeded in obtaining a direct and precise measurements from the rotational excitation of CO molecules. They constrained the deviation from linear scaling to be $\alpha = -0.007 \pm 0.027$ at $z \sim 3$. Battistelli et al. (2002) reported the first observations of $T(z)$ using the TSZ effect of the COMA and A2163 clusters of galaxies with $\alpha = -0.16^{+0.34}_{-0.32}$. Luzzi et al. (2009) determined the CMB temperature in the redshift range $z = 0.023 - 0.546$, from the measurements of 13 clusters. They restricted their analysis to $\alpha \in [0, 1]$ and set up an upper limit of $\alpha \leq 0.079$ at the 68% confidence level. No significant deviations from the redshift dependence of the CMB temperature predicted in the standard model has been found.

¹ Física Teórica, Universidad de Salamanca, 37008 Salamanca, Spain; email: ivan.demartino@usal.es; atrio@usal.es

² Centro de Astrofísica da Universidade do Porto, Rua das Estrelas s/n, 4150-762 Porto, Portugal; email: asilva@astro.up.pt; Carlos.Martins@astro.up.pt

³ Institute for Astronomy, University of Hawaii, 2680 Woodlawn Drive, Honolulu, HI 96822, USA; email: ebeling@ifa.hawaii.edu

⁴ SSAI and Observational Cosmology Laboratory, Code 665, Goddard Space Flight Center, Greenbelt, MD 20771, USA alexander.kashlinsky@nasa.gov

⁵ Department of Physics, University of California at Davis, 1 Shields Avenue, Davis, CA 95616, USA; email: kocevski@physics.ucdavis.edu

While there is interest in doing such observations as far back as possible (which one can do with spectroscopic methods), low-redshift measurements play an important role too. First, the two techniques are complementary with each other since they have different systematics and probe the adiabatic evolution of the Universe at different redshifts. Spectroscopic observations probe the matter era, roughly between redshifts $z = 2 - 4$, while TSZ probes the epoch of dark energy domination, $z \leq 1$. In particular, these measurements can shed light on the onset of dark energy domination; in many models this is associated with as a phase transition (Mortonson et al. 2009, Nunes et al. 2009) which could leave imprints in the $T(z)$ relation. Second, in models where photon number is not conserved, not only does the temperature-redshift relation change, but so does the distance duality relation (Etherington 1933), and these departures from the standard behavior are not independent. This link between the two relations requires information at all redshifts and will, when better datasets become available, be a powerful consistency test for the standard cosmological paradigm (Avgoustidis et al 2012).

The Planck mission has been designed to produce a full-sky survey of the CMB with unprecedented accuracy in temperature and polarization (Planck Collaboration 2011a). The instrument operates at nine frequencies logarithmically spaced in the range 30-857GHz. The in-flight performance of the High and Low Frequency Instruments have been described by the Planck HFI Core Team (2011a) and Mennella et al (2011). Due to its large frequency coverage, high resolution and low noise, is an optimal instrument for blind detection of clusters using the TSZ effect. The first clusters detected by PLANCK include 189 cluster candidates with signal-to-noise larger than 6 (Planck Collaboration 2011b). These SZ clusters are mostly at moderate redshifts (86% had $z < 0.3$) and span over a decade in mass, up to the rarest and most massive clusters with masses above $10^{15}M_{\odot}$. In this article we analyze how PLANCK data can be used to test the standard scaling relation of the CMB temperature with redshift. We use a two-fold approach: first, our pipeline is tested on simulated clusters drawn from a full hydrodynamical simulation; second, using a catalog of 623 clusters derived from ROSAT data and with well measured X-ray properties, we predict the accuracy that PLANCK measurements will reach using those clusters. In comparison with earlier analysis of Horellou et al (2005), we use a catalog of X-ray selected clusters and in our simulations, gas evolution is fully taken into account. Briefly, in Sec 2 we describe our methodology; in Sec 3 we discuss our data and simulations; in Sec 4 we explain our pipeline; in Sec 5 we present our results and in Sec 6 we summarize our main conclusions. The final goal of the paper is to forecast the accuracy with which PLANCK will constraint α for our cluster sample.

Planck Channel	1	2	3	4	5	6
Central frequency ν_0 /GHz	44	70	100	143	217	353
Frequency resolution $\Delta\nu$ (FWHM/GHz)	8.8	14	33	47	72	116
Angular resolution $\Delta\theta$ (FWHM/arcmin)	26.8	13.1	9.8	7.1	5.0	5.0
Noise per pixel $\sigma_{noise}/\mu K$ (Blue Book)	51	52	15	12	19	58
Noise per pixel $\sigma_{noise}/\mu K$ (in-flight performance)	109	96	14	9	13	49

TABLE 1

TECHNICAL DETAILS OF PLANCK CHANNELS USED IN THIS STUDY. THE NOISE PER PIXEL IN-FLIGHT PERFORMANCE CORRESPONDS TO 1 YEAR OF INTEGRATION.

2. METHODOLOGY.

Compton scattering of CMB photons by the hot Intra-Cluster (IC) gas induces secondary temperature anisotropies on the CMB radiation in the direction of clusters of galaxies. There are two components: the thermal (TSZ, Sunyaev & Zeldovich 1972) due to the thermal motion of the IC medium with temperature T_e and the kinematic (KSZ, Sunyaev & Zeldovich 1980) due to the motion of the cluster with speed \vec{v}_{cl} respect to the isotropic CMB frame. Neglecting relativistic corrections, the TSZ and KSZ contributions to the temperature anisotropy in the direction of a cluster \hat{n} are given by

$$\frac{T(\hat{n}) - T_0}{T_0} = \int \left[G(\nu) \frac{k_B T_e}{m_e c^2} + \frac{\vec{v}_{cl} \hat{n}}{c} \right] d\tau = G(\nu) y_c + \tau \frac{\vec{v}_{cl} \hat{n}}{c} \quad (1)$$

In this expression, $d\tau = \sigma_T n_e dl$ is the cluster optical depth and $n_e(l)$ the electron density evaluated along the line of sight l , σ_T is Thomson cross section, T_0 the current CMB mean temperature, k_B the Boltzmann constant, $m_e c^2$ the electron annihilation temperature, c the speed of light and ν the frequency of observation. The Comptonization parameter is defined as $y_c = (k_B \sigma_T / m_e c^2) \int n_e T_e dl$. Due to its frequency dependence $G(\nu)$, the TSZ is a distortion of the CMB spectrum. Its amplitude is independent on the cluster distance, making it a useful tool to detect clusters at high redshifts. All known astrophysical foregrounds have a different dependence with frequency so clusters can be clearly detected in CMB maps with enough frequency coverage. In the non-relativistic limit, $G(x) = x \coth(x/2) - 4$. The reduced frequency x is given by $x = h\nu(z)/kT(z)$ with $\nu(z)$ the frequency of a CMB photon scattered off by the IC gas and $T(z)$ the black body temperature of the CMB at the cluster location.

If the Universe evolves adiabatically, $T(z) = T_0(1+z)$. Due to the expansion, the frequency of a photon scattered by the IC plasma at redshift z is Doppler shifted as: $\nu(z) = \nu_0(1+z)$ and the ratio $x = h\nu(z)/kT(z) = h\nu_0/kT_0 = x_0$

is independent of redshift. If the evolution of the Universe is non-adiabatic, the temperature-redshift relation would not be constant. Two functional forms have been considered in the literature: $T(z) = T_0(1+z)^{1-\alpha}$ (Lima et al 2000) and $T(z) = T_0(1+bz)$ (LoSecco et al 2001). In both cases, the photon frequency is assumed to be redshifted as in the standard model: $\nu(z) = \nu_0(1+z)$. Since the largest fraction of known clusters of galaxies are at redshifts below $z \leq 0.7 - 1$, the differences between both redshift dependences are small so we will only analyze the first model. The reduced frequency varies as $x = x_0(1+z)^\alpha$ and the spectral frequency dependence of the TSZ effect, $G(\nu)$ now depends on α : $G(x) = G(\nu, \alpha)$. Using the TSZ effect, two methods have been proposed to constraint α . Fabbri et al. (1978) proposed to measure the zero cross frequency of clusters at different redshifts that, for adiabatic evolution, occurs at $\nu \simeq 217 \text{GHz}$. Rephaeli (1980) suggested to use the ratio of the TSZ anisotropy at different scales, $R(\nu_1, \nu_2, \alpha) = G(\nu_1, \alpha)/G(\nu_2, \alpha)$. Both methods have different systematics. By taking ratios, the dependence on the Comptonization parameter is removed and the need to account for model uncertainties on the gas density and temperature profile is avoided. At the same time, the analysis is more complicated since the distribution of temperature anisotropy ratios is highly non-gaussian (Luzzi et al. 2009). The measurement of the cross over frequency is also problematic since the TSZ is inherently weak and could be dominated by uncertain systematics. For this reason, the measurements carried out thus far (Battistelli et al 2002, Luzzi et al 2009), based in a small number of clusters, have concentrated in the ratio method. As an alternative to the zero frequency method, we will fit the TSZ signal at different frequencies and we will measure the function $G(\nu, \alpha)$. We shall denote this procedure the *Fit Method*.

The function $G(\nu, \alpha)$ characterizes uniquely the TSZ contribution. At each frequency, PLANCK Low Frequency Instrument (LFI) receivers and High Frequency Instrument (HFI) bolometers are sensitive to a wide range of frequencies and the spectral dependence is not $G(\nu)$ but

$$\bar{G}(\nu_0, \alpha) = \int_0^\infty G(\nu, \alpha) e^{(\nu-\nu_0)^2/2\sigma_\nu^2} d\nu \quad (2)$$

Hereafter, we will remove the upper bar and $G(\nu, \alpha)$ will refer to the averaged frequency dependence of eq (2). In Fig 1 we plot the temperature ratio (Fig 1a) and frequency dependence (Fig 1b) for different values of α . In Fig 1a, the solid line represents the adiabatic evolution model $\alpha = 0$ that is independent of redshift; the dot-dashed lines bound the region where $\alpha = -1, 1$. From top to bottom, the ratios are $R(\nu, 353 \text{GHz}, \alpha)$ with $\nu = 143, 100, 44 \text{GHz}$. In Fig 1b, we plot the spectral dependence $G(\nu, \alpha)$ for adiabatic evolution ($\alpha = 0$, dashed line) and $\alpha = -1, 1$ for a cluster at redshift $z = 0.1$ (dot-dashed line) and $z = 0.3$ (solid line). The null TSZ signal, represented by the dotted line, shows that the zero cross frequency varies in the range $\nu \sim 170 - 270 \text{GHz}$.

To construct a pipeline that implements the ratio or zero cross frequency tests we need to consider the specifics of the PLANCK data. The cosmological CMB signal is the dominant contribution except at the most massive clusters. Foreground residuals or astrophysical contaminants, while smaller in amplitude, would induce systematic shifts in the Comptonization parameter (Aghanim, Hansen & Lagache, 2005) varying with frequency and biasing the redshift dependence of the TSZ effect. To characterize the noise and foreground emission, the HFI and LFI core teams have constructed maps with the CMB cosmological contribution subtracted off the Time Ordered Information (TOI). They have used six different component separation algorithms to remove the primordial CMB signal. The difference between the six methods provides an estimate the CMB residual (Planck HFI Core Team 2011b, Zacchei et al 2011). The resulting maps are dominated by noise and foreground residuals. Due to the scanning strategy, the noise is rather inhomogeneous, largely dominated by a white noise component plus a $1/f$ contribution. In the LFI instrument, the $1/f$ noise is largest at 30GHz. For the HFI, the noise is largest at 545 and 857GHz. Also, those channels have the smallest resolution and we will not be considered in this work. Later we shall show that this is not a limitation since the channels with the highest resolution are the ones with the largest statistical power to determine α . The technical details of the maps considered in this study are listed in Table 1: central frequency and FWHM of the antenna spectral response function, approximated by a gaussian with FWHM $\Delta\nu$, angular resolution and noise per pixel. We indicate the required Blue Book specifications⁶) and the in-flight measured noise per pixel after one year of integration (Mennella et al 2011, Planck HFI Core Team 2011a). With respect to astrophysical contaminants, WMAP used the K, Ka Differencing Assemblies and the extinction corrected H α maps (Finkbeiner 2003) to subtract the synchrotron and free-free emissions and the Finkbeiner et al (1999) map to subtract the dust contribution (see Gold et al 2009 for details). A similar analysis using the 30, 545 and 857 GHz channels, and foreground templates could be used to remove the foreground contribution. Ideally, one would obtain maps without cosmological signal and with a low level of foreground residuals.

Maps free of the intrinsic CMB signal and/or foreground residuals are the most convenient to test the adiabatic evolution of the Universe. Removing the cosmological CMB signal on the TOI data leaves an unknown level of CMB residuals, whose distribution and power spectrum are difficult to model and the final results could be biased in an unmeasurable way. Alternatively, the intrinsic CMB can be removed by subtracting the highest resolution map, conveniently degraded, from the other maps. Both techniques have different systematics and the consistency of the results would be a test of their validity. Therefore, we shall carry out two type of simulations, depending on what data sets become available: (A) CMB subtraction in the TOI plus foreground removal using templates would produce maps with only instrumental noise, KSZ and TSZ with some unknown levels of primordial CMB and foreground residuals. Deviations from adiabatic evolution can be measured by taking ratios of temperature anisotropies at different frequencies (Fig 1a) or by fitting the spectral dependence $G(\alpha, \nu)$ (Fig 1b) to the data. (B) The component

⁶ [http://www.rssd.esa.int/SA/PLANCK/docs/Bluebook-ESA-SCI\(2005\)1_V2.pdf](http://www.rssd.esa.int/SA/PLANCK/docs/Bluebook-ESA-SCI(2005)1_V2.pdf)

separation takes place on the final maps. The primordial CMB is removed using the foreground clean 217GHz map. We degrade the angular resolution of the 217GHz channel to that of the other 5 channels before subtracting it from the corresponding map. We checked that the intrinsic CMB and KSZ anisotropies are removed exactly but the frequency dependence of the TSZ effect is modified. In Fig 2a, we plot the ratio of the CMB-KSZ removed maps at different frequencies: $R_{[-217GHz]}(\nu_1, \nu_2, \alpha) = [G(\nu_1, \alpha) - G(217GHz, \alpha)]/[G(\nu_2, \alpha) - G(217GHz, \alpha)]$. In Fig 2b we represent $G_{[-217GHz]}(\nu, \alpha) = G(\nu, \alpha) - G(217GHz, \alpha)$. The lines follow the same conventions than in Fig. 1.

Our pipeline will analyze maps using CMB subtraction on the TOI (method A) and on the maps themselves (method B). We will compute α with both the ratio and the fit method. By subtracting the 217GHz, the estimator $R_{[-217GHz]}$ has a much weaker dependence on α than R . With respect to the fit method, we do not measure $G(\nu, \alpha)$ directly but $\Delta T(\hat{n}) = T_0 y_c G(\nu, \alpha)$. To measure the spectral shape from the data we need an independent determination of y_c using X-ray data. We will use a proprietary catalog of X-ray selected clusters with all the required information (see Sec. 3.1) and for this catalog we will forecast the constrain to be achieved with PLANCK.

3. CLUSTER TEMPLATES AND FINAL MAPS.

To test our systematics, we will construct two TSZ templates: one based on our catalog of X-ray selected clusters, the other based on an all-sky hydrodynamical simulation. The final maps were simulated using the HealPix package (Gorski et al 2005) with resolution $N_{side} = 1024$.

3.1. Y-map from X-ray selected clusters.

Our cluster sample contains 623 clusters outside WMAP Kp0 mask. It was created combining the ROSAT-ESO Flux Limited X-ray catalog (REFLEX, Böhringer et al 2004) in the southern hemisphere, the extended Brightest Cluster Sample (eBCS, Ebeling et al 1998, Ebeling et al 2000) in the north, and the Clusters in the Zone of Avoidance (CIZA, Ebeling, Mullis & Tully 2002, Kocevski et al 2007) sample along the Galactic plane. All three surveys are X-ray selected and X-ray flux limited. A detailed description of the creation of the merged catalog is given in Kocevski & Ebeling (2006). The position, flux, X-ray luminosity and angular extent of the region containing the measured X-ray flux were determined directly from ROSAT All Sky Survey (RASS). All clusters have spectroscopically measured redshifts. The X-ray temperature was derived from the $L_X - T_X$ relation of White, Jones & Forman (1997). The central electron densities and core radii were derived by fitting to the RASS data a spherically symmetric isothermal β model (Cavaliere & Fusco-Femiano 1976) convolved with the RASS point-spread function. The β was fixed at the canonical value of 2/3 to reduce the dependence of the β model parameters with the choice of radius over which the model is fit. These data allows to compute the Comptonization parameter at the center of the cluster.

Atrio-Barandela et al (2008) compared the TSZ predicted from the X-ray data with the signal present in WMAP 3yr data and found it to be in good agreement within the X-ray emitting region, where the β model is a good description of the electron distribution. In the cluster outskirts, the TSZ signal was systematically higher than the measured value. The latter was consistent with the Komatsu & Seljak (2002) profile, where baryons are in hydrostatic equilibrium within a dark matter halo well described by a Navarro-Frenk-White profile (hereafter NFW, Navarro, Frenk & White 1997), as expected in the concordance Λ CDM model. More recently, Nagai et al (2007) proposed a scaled 3-dimensional electron pressure profile $p(x) = P_e(r)/P_{500}$ based on a generalizad NFW profile

$$p(x) = \frac{P_0}{(c_{500}x)^\gamma [1 + (c_{500}x)^\alpha]^{(\beta-\gamma)/\alpha}}, \quad (3)$$

where (γ, α, β) are the central, intermediate and outer slopes, c_{500} characterizes the gas concentration and $x = r/R_{500}$ is the radius at which the average density of the cluster is 500 times the critical density. Arnaud et al (2010) derived an average cluster pressure profile from observations of a sample of 33 local ($z < 0.2$) clusters, scaled by mass and redshift with

$$[P_0, c_{500}, \gamma, \alpha, \beta] = [8.403h_{70}^{-3/2}, 1.177, 0.3081, 1.0510, 5.4905] \quad (4)$$

Later, Plagge et al (2010) showed these parameters to be consistent with the SZ measurements of 15 massive X-ray clusters observed with the South Pole Telescope (Plagge et al 2010). We determine the scale R_{500} using (Böhringer et al 2007)

$$R_{500} = \frac{(0.753 \pm 0.063)h^{-1} \text{ Mpc}}{h(z)} \left(\frac{L_X}{10^{44}h^{-2} \text{ erg s}^{-1}} \right)^{0.228 \pm 0.015} \quad (5)$$

To test the effect of the cluster profile on the final results, we construct y-maps from the X-ray cluster catalog (a) using the universal pressure profile of eq. (3) with the parameters given in eq. (4) and (b) using the isothermal $\beta = 2/3$ model. The Comptonization parameter is computed integrating the electron pressure profile along the line of sight. Clusters are assumed to be spherically symmetric and extending up to R_{200} , the scale where the cluster overdensity reaches 200 times the critical density. To determine the effect of the cluster profile, the central value of y_c is assumed to be the same. Finally, the cluster templates are convolved with the corresponding antenna beams (see Table 1). In the Fig. 3a we show the pressure profile integrated along of line of sight for the $\beta = 2/3$ (solid line) and universal pressure (dashed line) profiles convolved with the antenna of the 44GHz map. The cluster is located at $z = 0.094$, of

$M_{500} = 2.4 \times 10^{14} h^{-1} M_{\odot}$ and $R_{500} = 746 h^{-1} \text{Kpc}$. For illustration, in Fig. 3b we plot the value of Comptonization parameter y_c at the center of all the clusters in our proprietary cluster catalog, derived using the measured X-ray parameters, as a function of cluster mass. The solid line represents the linear regression fit to the data. The central Comptonization parameter scales as: $y_c = 24.5 (M_{500}/10^{14} h^{-1} M_{\odot})^{1.35}$.

3.2. Y-map from simulated clusters.

As an alternative, we also use the low-redshift all-sky maps and the associated galaxy cluster catalogues of the *hydrodynamic* diffuse and kinetic SZ simulations included in the *pre-launch Planck Sky Model*. The simulations are fully described in Dellabrouille et al (2011). The catalogues contain cluster positions, mass and radius for an overdensity contrast of 200 times the critical density. The maps contain the integrated SZ signal up to $z \simeq 0.25$, computed from a combination of full hydrodynamic simulations using the box staking method described in Valente, da Silva & Aghanim (2012). According to this method, the Universe around the observer is generated in concentric layers, each with a comoving thickness of $100 h^{-1} \text{Mpc}$, using the outputs of hydrodynamic simulations with periodic boundary conditions. The light-cone integrations of the TSZ and KSZ signals are carried out using the formulae in da Silva et al (2000) and (2001). A total of seven layers were constructed, up to $z=0.25$. The innermost layer includes the local constrained simulation of Dolag et al (2005), whereas all the other layers were produced from gas snapshots of the ΛCDM simulation in De Boni et al (2010). Both these simulations include explicit treatment for gas cooling, heating by UV, star formation and feedback processes.

The y-map constructed from the X-ray selected clusters assumes clusters to be spherically symmetric and relaxed while the TSZ and KSZ templates constructed from the hydrodynamic simulation contains clusters with different dynamical state (relaxed, merging systems, etc), shape and ellipticity. Also, since the latter are constructed integrating the signal along the line of sight, the projection effects due to low mass clusters and groups are included. Therefore, these templates are very well suited to study the effect of all these systematics and of the KSZ component in the determination of α . For a more realistic comparison, we select 623 clusters from the simulation according to the measured selection function of the X-ray cluster sample. In Fig 4a we plot the mass and in Fig 4b the redshift distribution of all clusters in our simulation (solid line) that fulfill the selection criteria. The dashed line shows the same distributions of the X-ray clusters. For a better comparison, the histogram of largest amplitude was normalized to unity. The main difference between the two samples is that there are 22 clusters in our proprietary cluster catalog that have redshifts larger than $z = 0.25$, the redshift of the last layer constructed from the simulation.

3.3. Final Maps.

The y-maps described above are multiplied by $G(\nu, \alpha = 0)$ to generate TSZ templates and convolved with the antenna beam. A KSZ template was added to the hydrodynamical but not to the X-ray selected cluster template since their peculiar velocity is not available. Noise maps were constructed assuming the Blue Book noise levels of Table 1. When presenting our results, we shall demonstrate that the HFI frequencies have the largest statistical power to constrain α . We model the noise as homogeneous and uncorrelated white noise since at the frequencies 44 – 353GHz the $1/f$ is both small and does not affect the angular scales subtended by clusters, $\ell \sim 500$ and above.

To take into account the two different component separation techniques, we carry out two different set of simulations: in (A) the CMB is removed in the TOI. Maps will only contain instrumental noise, TSZ and KSZ. In total, six different maps, one for each frequency of Table 1 are simulated. In (B) the 217GHz map is used to remove the intrinsic CMB. Then, only five difference maps will be available for the analysis. Those maps will contain instrumental noise and TSZ, but the frequency dependence of the TSZ effect changes. More realistic simulations would include foreground residuals, noise inhomogeneities with an $1/f$ component that can only be accurately model once the data becomes available. However, we do not expect that our results obtained with our simplified maps will change with more realistic simulations if noise inhomogeneities are uncorrelated with the cluster distribution. Then, we constructed two set of maps, according to the specific simulation. In simulation (A) six maps, one for each frequency of Table 1, are constructed by adding noise to the TSZ and KSZ templates. The temperature anisotropy at each pixel is: $\Delta T_A(\nu) = y_c G(\nu, 0) + \Delta T_{KSZ} \pm \sigma_{noise, \nu}^A$. In simulation (B) six maps are constructed adding cosmological CMB signal and noise to the cluster templates. The 217GHz map is used to subtract the cosmological and KSZ signals. Therefore, only five different maps are available for the analysis. We checked the final maps had a power spectrum that was a pure white noise, with a slightly larger variance $\sigma_{noise, \nu}^B$, sum of the original map plus the noise of the degraded 217GHz map. At each pixel, the temperature anisotropy is: $\Delta T_B(\nu) = y_c G_{[-217\text{GHz}]}(\nu, 0) \pm \sigma_{noise, \nu}^B$. We neglect relativistic corrections that are only significant for the most massive clusters (Nozawa et al 1998).

4. DATA PROCESSING.

In both simulations A and B, we construct estimators using both the Ratio and the Fit methods. To simplify the notation, let the index $I = (A, B)$ denote the type of simulation and let us redefine $G_A = G(\nu, \alpha)$, $R_A = R(\nu_1, \nu_2, \alpha)$, $G_B = G_{[-217\text{GHz}]}(\nu, \alpha)$ and $R_B = R_{[-217\text{GHz}]}(\nu_1, \nu_2, \alpha)$. At each cluster location, projection effects can yield contributions from different redshifts altering the frequency dependence. To reduce the effect, we will take averages over the cluster extent. The temperature anisotropy is then

$$\langle \Delta T_I(\nu_1) \rangle = \bar{y}_c G_I(\nu_1) \pm \sigma_{noise, \nu_1}^I / \sqrt{N_{pix}}. \quad (6)$$

where N_{pix} is the number of pixels occupied by the cluster. There will be an extra KSZ component for simulation A.

4.1. Ratio method.

To estimate α we compute the likelihood

$$-2 \log \mathcal{L} = \sum_{\nu_1, \nu_2} \sum_{i=1}^{N_{cl}} \left[\frac{\langle \Delta T_I(\nu_1) \rangle / \langle \Delta T_I(\nu_2) \rangle - R_I(\nu_1, \nu_2, \alpha)}{\sigma_{ratio,i}^I} \right]^2 \quad (7)$$

for different values of α . A few examples of $R_I(\nu_1, \nu_2, \alpha)$ are plotted in Fig 1a and 2a. In eq. (7), we compute $\sigma_{ratio,i}^I$ for each cluster as the rms deviation of 1,000 simulations of the ratio $\langle \Delta T_I(\nu_1) \rangle / \langle \Delta T_I(\nu_2) \rangle$ where the TSZ component is held fixed to the actual value at the cluster location and the noise is drawn from a gaussian distribution with zero mean and variance $(\sigma_{noise,\nu}^I)^2 / N_{pix,i}$. As discussed in Luzzi et al (2009) the distribution of ratios is dominated by the error on the denominator. Therefore, in our simulations type (A) we exclude the 217GHz channel from the denominator, where the TSZ signal is null, to minimize the bias.

4.2. Frequency fit method.

Alternatively, we can fit the TSZ signal of each cluster to the spectral dependence of Fig 1b and 2b. Similarly, the likelihood function is

$$-2 \log \mathcal{L} = \sum_{\nu} \sum_{i=1}^{N_{cl}} \left[\frac{\langle \Delta T_I(\nu) \rangle - \bar{y}_c G_I(\nu, \alpha)}{\sigma_{noise,\nu,i}^I} \right]^2, \quad (8)$$

where $\sigma_{noise,\nu,i}^I = \sigma_{noise,\nu}^I / \sqrt{N_{pix,i}}$.

This method requires an independent estimate of y_c , introducing another complication. As is indicated in Table 1, different frequencies have different resolutions. The cluster anisotropies are diluted by the antenna beam and the TSZ signal does not scale as $G_I(\nu, 0)$. As an example, in Fig 5 open squares represent the average TSZ amplitude on the 5 difference maps $\Delta T_{[\nu, -217GHz]}$; the solid line represents their frequency dependence $G_{[-217GHz]}(\nu, 0)$ of Fig 2b. Due to the antenna, the measured TSZ signal of the clusters differs from the expected scaling. The effect is most noticeable at 44GHz since this channel has the smallest resolution. The amplitude of the effect depends on the cluster profile and angular extent *but does not depend on the scaling of the TSZ signal with redshift*, $G(\nu, \alpha)$. Fig 5a corresponds to a cluster at redshift $z = 0.218$, with mass $M_{500} = 3.64 \times 10^{14} M_{\odot}/h$ and size $9.4'$ while in Fig 5b the cluster is located at $z = 0.058$ with mass $M_{500} = 7.7 \times 10^{14} M_{\odot}/h$ and size $42'$.

For clusters drawn from a simulation, its size, ellipticity and profile are known exactly. For such clusters, the deconvolution factor F can be determined exactly by comparing the average Comptonization parameter before ($\langle y_c \rangle$) and after ($\langle y_c * B(\nu) \rangle$) convolving with the antenna beam $B(\nu)$: $F = \langle y_c \rangle / \langle y_c * B(\nu) \rangle$. This factor would be different for resolved and unresolved clusters and would depend on the cluster profile and redshift. For X-ray selected clusters, we know the Comptonization parameter in the cluster cores but their pressure profile has not been measured. This will introduce an extra uncertainty when comparing the measured TSZ effect with the theoretical prediction. For illustration, in Fig 6a we represent F for a sample of 110 clusters in the mass range $M_{500} = 5 - 6 \times 10^{14} M_{\odot}/h$. In Fig 6b, we plot the deconvolution factors for all clusters in our simulation with masses $M_{500} \geq 10^{15} M_{\odot}/h$. Solid black circles correspond to the 353GHz frequency and open squares to 44GHz. All clusters are resolved at 353GHz. At 44GHz clusters with redshift $z \geq 0.08$ are unresolved. For clarity the clusters at lower redshift, that would be resolved, are not shown.

In Fig 6 the solid straight lines correspond to the linear regression fit to the deconvolution factor for each cluster mass range and channel. Arrows indicate the deconvolution factor of the clusters plotted in Fig 5a,b. If for each redshift, frequency and mass range, F_{lin} is the deconvolution factor estimated by the linear regression, F the true deconvolution factor and ΔF is the rms dispersion of the true deconvolution values F around F_{lin} for each mass bin and antenna, then $F = F_{lin} \pm \Delta F$. If for a real cluster we use F_{lin} instead of the (unknown) true factor F , the deconvolved signal $(\Delta T_{TSZ} * B) F_{lin}$ would differ from the true signal ΔT_{TSZ} by an amount $(\Delta T_{TSZ} * B) \Delta F$. This uncertainty is uncorrelated with the instrumental noise at the cluster location and can be included in the Likelihood analysis of eq. 8 by adding it in quadrature with the instrumental noise: $\sigma_{tot,i}^2 = \sigma_{noise,i}^2 + [(\Delta T_{TSZ} * B) \Delta F]^2$. On the other hand, the deconvolution coefficient does not scale linearly with redshift, and F_{lin} underestimates the true deconvolution factor F especially at high redshifts, potentially biasing our estimation of α . We used the y-map computed with clusters drawn from a numerical simulation to compute the deconvolution factors F_{lin} and its uncertainty ΔF in three mass bins of equal number of clusters: $M_{500} \leq 2 \times 10^{14} M_{\odot}/h$, $M_{500} = 2 - 3.6 \times 10^{14} M_{\odot}/h$ and $M_{500} \geq 3.6 \times 10^{14} M_{\odot}/h$. The deconvolution factors, that were different for resolved and unresolved clusters, were used to deconvolve the templates of simulated and of X-ray clusters.

5. RESULTS AND DISCUSSION

We first tested the ratio and fit methods using the template constructed from simulations, as described in Sec. 3.2. The template contained a subset of 623 clusters distributed in mass and redshift according to the cluster catalog selection function (see Fig 4) and included both TSZ and KSZ components. Second, we repeated the analysis with the template of X-ray selected clusters. No KSZ contribution was added in this case. The first and most important conclusion is that we found no significant differences from the results computed using both templates, implying that the effect of KSZ, cluster dynamical state and deviations from spherical symmetry are averaged out over such a large cluster sample, effects that were important when analyzing observations of just a few clusters (Battistelli et al 2002, Luzzi et al 2009).

With respect to the method of analysis, the ratio method performs differently if the CMB is removed in the TOI (method A) or in the final map (method B) but the differences are small for the fit method. For the ratio method, we will only present results obtained with the simulated cluster template and simulation type (A) (Fig 7). For the fit method, the results presented are only using the template constructed from X-ray selected clusters and simulation type (B) (Fig 8) and we will discuss all the other cases. To test the importance of the different contributions, we define three mass bins $M_{500} = ([< 0.192], [0.192 - 0.365], [> 0.36]) \times 10^{15} M_{\odot}/h$ of equal number (~ 208) of clusters, and three redshift bins $z = ([< 0.11], [0.11 - 0.17], [> 0.17])$ with mean redshift $\langle z \rangle = (0.08, 0.14, 0.20)$, also with the same number of clusters. We computed the likelihood (eqs. [7] and [8]) for the different mass and redshift bins and different frequencies to determine the data subset with the largest statistical power. To compute likelihoods, we subdivide the interval $\alpha = [-1, 1]$ in 2001 steps. We perform 1,000 Monte-Carlo simulations for each cluster template, simulation type and method.

5.1. Ratio method.

Our results indicate that the ratio method is strongly biased. The likelihood function is dominated by the few clusters where the TSZ signal is erased by the noise so $\langle \Delta T(\nu_2) \rangle \sim 0$ in the denominator of eq. (7), biasing the results towards negative values of α . We found this bias is removed by rejecting all ratios where the denominator is smaller than $0.2\sigma_{noise}^A$. This constrain rejects 5% of the data but reduces the bias to insignificant levels. In Fig. 7 we present the likelihood function of a single simulation randomly selected of our ensemble of 1,000 simulations. In Fig. 7a we represent the likelihood for clusters within the three redshift bins given above, marginalized over cluster mass and 15 frequency ratios. Dashed, dot-dashed and solid lines correspond to the lower, intermediate and high redshift bins. In Fig. 7b we present the results binning clusters according to mass. Dashed, dot-dashed and solid correspond to lower, intermediate and high mass bin. As expected, the most massive clusters dominate the likelihood. The final value obtained in this single simulation is $\alpha = 0.0 \pm 0.012$. In Fig. 7c we plot the histogram distribution of the α values measured in 1,000 simulations. Solid line represents the results for simulation type A where $\langle \alpha \rangle = -0.003 \pm 0.011$. Our pipeline is marginally biased since the mean of our simulations $\langle \alpha \rangle = -0.003$ differs from $\alpha = 0$ by more than $\sigma_{\alpha}/\sqrt{N_{sim}} = 3.5 \times 10^{-4}$. For comparison, in Fig. 7c the dashed line corresponds to simulation type B. The value of α averaged over all simulations is $\langle \alpha \rangle = -0.19 \pm 0.18$. In this case, the larger uncertainty reflects the weak dependence of the ratio method with α , as shown in Fig 2a. Finally, we also checked that ratios using lower resolution maps have less statistical power to constrain α . In retrospect, this justifies neglecting the 30, 545 and 857GHz channels, with large noise levels or (1/f) contributions, that would complicate the analysis without adding more information.

5.2. Fit method.

The results of the fit method using a template of X-ray clusters and simulations type B are presented in Fig. 8. The cluster template was constructed using the universal pressure profile of eq. 3, with the parameters given in eq. 4. In (a) we plot the likelihood function for three different frequencies: 44GHz (dashed), 100 GHz (solid) and 343GHz (dot-dashed line). The figure shows that the 100GHz channel is the most restrictive of the three. Like for the ratio method, the final likelihood is dominated by the channels that have high resolution and low noise, in this case the 100 and 143GHz channels. In Fig. 8b we represent the likelihood for the three mass bins given above and marginalized over frequencies; dashed, dot-dashed and solid lines correspond to the low, intermediate and high mass intervals. The signal is dominated by the most massive clusters that, on a flux limited sample, are on average at high redshift than the lower and intermediate mass samples. For this particular realization, the estimated value is $\alpha = 0.013 \pm 0.020$, compatible with adiabatic evolution at the 1σ level.

In Fig. 8c we represent the histograms of 1,000 simulations together with their linear fits for cluster templates constructed using the universal pressure profile (dot-dashed line) and the $\beta = 2/3$ (solid line). The mean and rms dispersion of the estimated values are $\langle \alpha \rangle = -0.013 \pm 0.016$ for the universal profile and $\langle \alpha \rangle = 0.003 \pm 0.008$ for the β -model profile. When all cluster properties are identical, the TSZ integrated over the cluster extent will be larger for the β -model than for the universal profile (see Fig 3a) so it must constrain α better, as shown. We also carried out 1,000 simulations using method A, that does not include the intrinsic CMB signal, with the hydrodynamical template, that contains the KSZ component. The result was $\langle \alpha \rangle = -0.008 \pm 0.015$, identical to the result with the method B above. Therefore, in the fit method is not so important to have maps with the cosmological signal removed as, for example, in the ratio method. Using the 217GHz map to remove the intrinsic CMB signal alters the TSZ frequency dependence, but the TSZ signal is still strongly dependent with redshift (see Figs. 1b and 2b) what is not the case in the ratio method (compare Figs. 1a and 2a).

Let us remark that the rms dispersion of α on 1,000 simulations, σ_{α} , is very similar to the error on α in one single

realization, both in the ratio and in the fit method, indicating that our pipelines are efficient. The results obtained using y-maps constructed with clusters drawn from a hydrodynamical simulation or from a catalog of X-ray selected clusters show no significant differences. In the hydro-simulation, the y-map integrates the SZ signal up to $z \simeq 0.25$ and contains all the projection effects up to that redshift, not included in the X-ray selected clusters template, we can conclude that projection effects play no significant role. This can be understood in the light of the results presented in Fig 8b; the full likelihood is dominated by the most massive clusters for which projection effects are not significant (Valente et al 2012).

6. CONCLUSIONS.

Planck offers an excellent opportunity to constrain the evolution history of the CMB blackbody temperature with better precision than quasar excitation lines using currently available X-ray cluster catalogs. We have found that taking the ratio of temperature anisotropies at different frequencies is strongly biased but this bias can be corrected by rejecting all ratios where the denominator is much smaller than the noise. Fitting the frequency dependence provides an equally reliable estimator with different systematics but requires both an independent determination of the Comptonization parameter and deconvolution of the antenna beam. The latter can not be done exactly if the cluster pressure profile is not known precisely. We have shown that deconvolution using linear fits introduces an error that can be easily incorporated into the analysis.

We have considered two possible methods to remove foregrounds and the cosmological CMB signal and the KSZ contribution: the cosmological signal is removed in the TOI and the 217GHz map is used to remove the cosmological and KSZ signal exactly. We have carried out simulations of both methods to investigate the differences on the final results. We have shown that the ratio method performs rather well if the cosmological CMB signal is clean in the TOI but very badly otherwise. The fit method performs equally well in both data sets, giving results that are only marginally biased. With both methods, massive clusters and the high resolution/low noise channels have the largest statistical power to constrain α . We have used a proprietary cluster catalog that contains spectroscopic redshifts and all the required X-ray information to estimate the accuracy that would be achieved with Planck data. We forecast that the final uncertainty will be about $0.011 - 0.016$ a factor 2-3 better than those obtained from quasar spectra by Noterdaeme et al (2010), depending on what type of Planck data becomes publicly available.

Since our catalog is restricted to clusters with $z \leq 0.3$, we have not extended our analysis beyond that redshift. Planck has already detected around 200 clusters with a $S/N \geq 10$, one at $z \simeq 0.94$ with $M_{500} \simeq 8 \times 10^{14} M_{\odot}$. Adding more clusters with current or future experiments will help to detect possible deviations from adiabatic evolution, specially if clusters are of higher mass and are at a higher redshift like the one recently reported in Planck Collaboration 2011c. Once all PLANCK and South Pole cluster candidates have been observed on the X-ray and their redshift determined, the measurements proposed will provide much stronger constraints on non-adiabatic evolution, than those quoted here.

7. ACKNOWLEDGEMENTS

This work was done in the context of the FCT/MICINN cooperation grant 'Cosmology and Fundamental Physics with the Sunyaev-Zel'dovich Effect' AIC10-D-000443, with additional support from project PTDC/FIS/111725/2009 from FCT, Portugal and FIS2009-07238 and CSD 2007-00050 from the Ministerio de Educación y Ciencia, Spain. The work of CM is funded by a Ciência2007 Research Contract, funded by FCT/MCTES (Portugal) and POPH/FSE (EC).

REFERENCES

- Aghanim, N., Hansen, S.H. & Lagache, G. 2005, *A&A*, 439, 901
 Arnaud, M., Pratt, G. W., Piffaretti, R., Böhringer, H., Croston, J. H., Pointecouteau, E. 2010, *A&A*, 517, 92
 Atrio-Barandela, F., Kashlinsky, A., Kocevski, D., Ebeling, H. 2008, *Astrophys J*, 675, L57
 Avgoustidis, A., Luzzi, G., Martins, C.J.A.P. & Monteiro, A.M.R.V.L., 2012 JCAP, in press. Preprint arXiv:1112.1862
 Bahcall, J. N. & Wolf, R. A. 1968, *ApJ*, 152, 701
 Battistelli, E. S. et al. 2002, *Astrophys J*, 580, L101
 Böhringer, H. et al. 2004, *A&A*, 425, 367
 Böhringer, H. et al. 2007, *A&A*, 469, 363
 Cavaliere, A. & Fusco-Femiano, R. 1976, *A&A*, 49, 137
 da Silva A., Barbosa D., Liddle A., Thomas P., 2000, *MNRAS*, 317, 37
 da Silva A., Barbosa D., Liddle A., Thomas P., 2001, *MNRAS*, 326, 155
 De Boni C., Dolag K., Ettori S., Moscardini L., Pettorino V., Baccigalupi C., 2011, *MNRAS*, 415, 2758
 "The pre-launch Planck Sky Model: a model of sky emission at submillimetre to centimetre wavelengths." Delabrouille et al, 2012, in progress. (see details in <http://www.apc.univ-paris7.fr/~delabrou/PSM/psm.html>)
 Dolag K., Hansen F.K., Roncarelli M., Moscardini L., 2005, *MNRAS*, 363, 29
 Ebeling, H., Edge, A.C., Böhringer, H., Allen, S.W., Crawford, C.S., Fabian, A.C., Voges, W. & Huchra, J.P. 1998, *MNRAS*, 301, 881
 Ebeling, H., Edge, A.C., Allen, S.W., Crawford, C.S., Fabian, A.C. & Huchra, J.P. 2000, *MNRAS*, 318, 333
 Ebeling, H., Mullis, C.R. & Tully, R.B. 2002, *ApJ*, 580, 774
 Etherington, J.M.H., 1933, *Phil. Mag.*, 15, 761.
 Fabbri, R., Melchiorri, F., & Natale, V. 1978, *Astrophys. Space Sci.*, 59, 223
 Finkbeiner, D.P., Davis, M. & Schlegel, D.J. 1999, *ApJ*, 524, 867
 Finkbeiner, D.P. 2003, *ApJS*, 146, 407
 Gold, B. et al. 2009, *ApJS*, 180, 265
 Gorski, K. et al 2005, *Ap.J.*, 622, 759

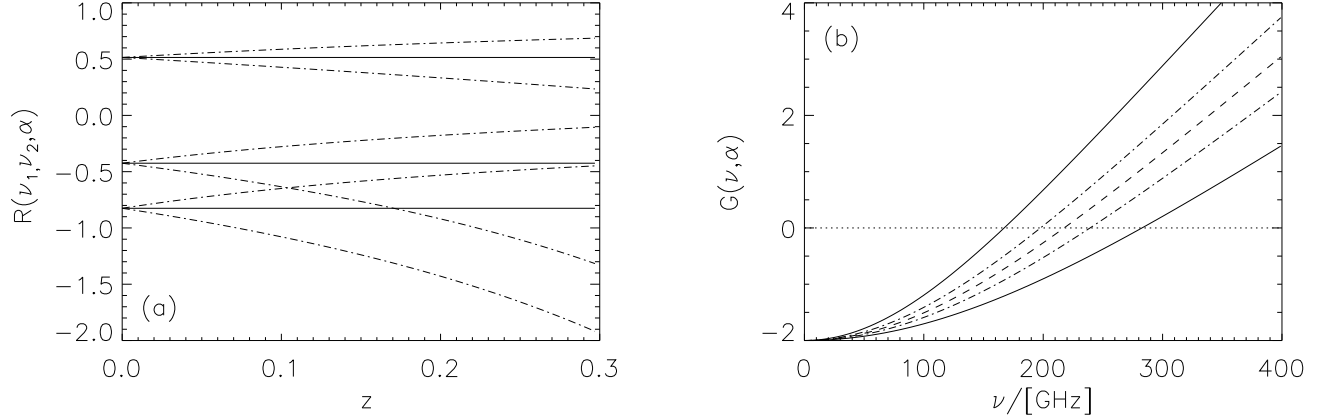


FIG. 1.— (a) variation of the ratio $R(\nu, 353\text{GHz}, \alpha)$ as a function of redshift for $\nu = 143\text{GHz}$ (top set of curves), 100GHz (middle set) and 44GHz (lower set). The solid straight line corresponds to adiabatic evolution $\alpha = 0$ and the dot-dashed lines represent $\alpha = -1, 1$. (b) Spectral dependence of the TSZ effect $G(\nu, \alpha)$ for two clusters located at two clusters located at $z=0.3$ (solid lines) and $z=0.1$ (dot-dashed lines) with $\alpha = -1, 1$. The dashed line corresponds to adiabatic evolution $\alpha = 0$, that is identical for any redshift. The zero cross frequency occurs when those lines cross the dotted line.

- Horellou, C., Nord, M., Johansson, D., Lévy, A. 2005, *Astron & Astrophys*, 441, 435
- Jetzer, P., Puy, D., Signore, M., & Tortora, C. 2011, *Gen. Rel. & Grav.*, 43, 1083
- Jetzer, P. & Tortora, C. 2012, preprint arXiv:1202.2248
- Kocevski, D.D. & Ebeling, H. 2006, *ApJ*, 645, 1043
- Kocevski, D.D., Ebeling, H., Mullis, C.R. & Tully, R.B. 2007, *ApJ* 662, 224
- Komatsu, E., & Seljak, U. 2002, *MNRAS*, 336, 1256
- Lima, J. A. S., Silva, A. I., & Viegas, S. M. 2000, *MNRAS*, 312, 747
- LoSecco, J. M., Mathews, G. J., & Wang, Y. 2001, *Phys. Rev. D*, 64, 123002
- Luzzi, G., Shimon, M., Lamagna, L., et al. 2009, *ApJ*, 705, 1122
- Mather, J.C. et al. 1999, *Astrophys J*, 512, 511
- “Planck early results. III. First assessment of the Low Frequency Instrument in-flight performance”. Mennella, A. et al, 2011, *A& A*, 536, A3
- Matyjasek 1995, *Phys. Rev. D*, 51, 4154
- Mortonson, M., Hu, W. & Huterer, D. 2009, *Phys. Rev. D*, 80, 067301
- Nagai, D., Kravtsov, A. V., & Vikhlinin, A. 2007, *ApJ*, 668, 1
- Navarro, J.F., Frenk, C.S., & White, S.D.M. 1997, *ApJ*, 490, 493
- Noterdaeme, P. et al. 2010, *MNRAS*, 403, 906
- Nozawa, S., Itoh, N., & Kohyama, Y. 1998, *ApJ*, 508, 17
- Nunes N.J., Dent T., Martins C.J.A.P. & Robbers G., 2009, *Mem. Soc. Ast. It.*, 80, 785
- Overduin, J. M., & Cooperstock, F. I. 1998, *Phys. Rev. D*, 58, 043506
- “Planck early results. I. The Planck mission”. Planck Collaboration 2011a, *A& A*, 536, A1
- “Planck early results. VIII. The all-sky early Sunyaev-Zeldovich cluster sample”. Planck Collaboration 2011b, *A& A*, 536, A8
- “Planck early results. XXVI. Detection with Planck and confirmation by XMM-Newton of PLCK G266.6-27.3, an exceptionally X-ray luminous and massive galaxy cluster at $z \sim 1$ ”. Planck Collaboration 2011c, *A& A*, 536, A26
- “Planck early results. IV. First assessment of the High Frequency Instrument in-flight performance”. Planck HFI Core Team 2011a, *A&A* 536, A4
- “Planck early results. VI. The High Frequency Instrument data processing”. Planck HFI Core Team 2011b, *A&A* 536, A6
- Plagge, T. et al. 2010, *ApJ*, 716, 1118
- Puy, D. 2004, *A& A*, 422, 1
- Rephaeli, Y. 1980, *ApJ*, 241, 858
- Songaila, A., Cowie, L. L., Hogan, C. J., & Rugers, M. 1994, *Nature*, 368, 599
- Srianand, R., Petitjean, P., & Ledoux, C. 2000, *Nature*, 408, 931
- Sunyaev, R. A., & Zeldovich, Y. B. 1972, *Comments on Astrophys. Space Phys.*, 4, 173
- Sunyaev, R. A., & Zeldovich, I. B. 1980, *MNRAS*, 190, 413
- Valente, da Silva, A., Aghanim, N., 2012, in preparation
- White, D.A., Jones, C., Forman, W. 1997, *MNRAS*, 292, 419
- “Planck early results. V. The Low Frequency Instrument data processing”. Zacchei, A. et al. 2011, *A& A*, 536, A5

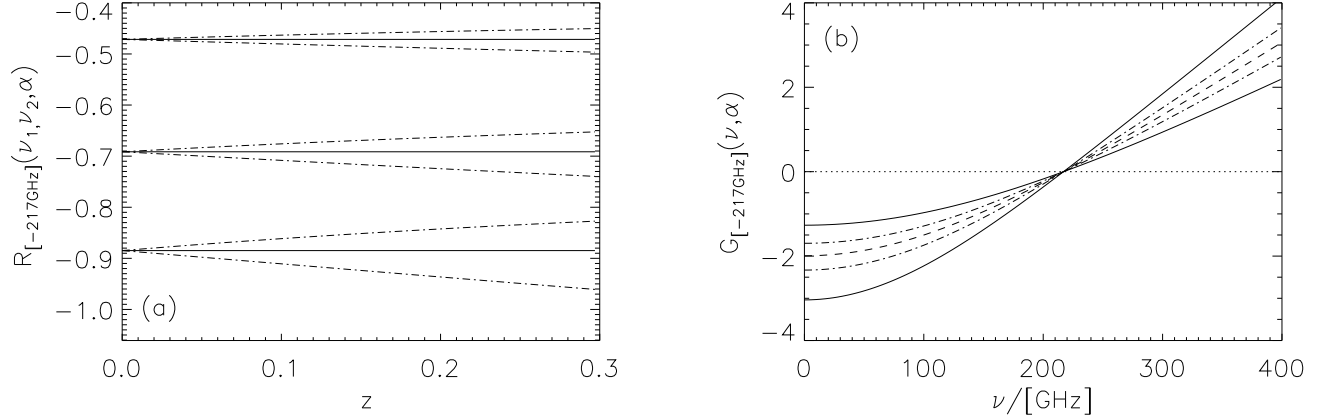


FIG. 2.— (a) Ratio $R_{[-217\text{GHz}]}(\nu, 353\text{GHz}, \alpha)$ for $\nu = 143, 100$ and 44GHz , and (b) Spectral dependence of $G(\nu, \alpha) - G(217\text{GHz}, \alpha)$. Curves follow the same convention as in Fig. 1.

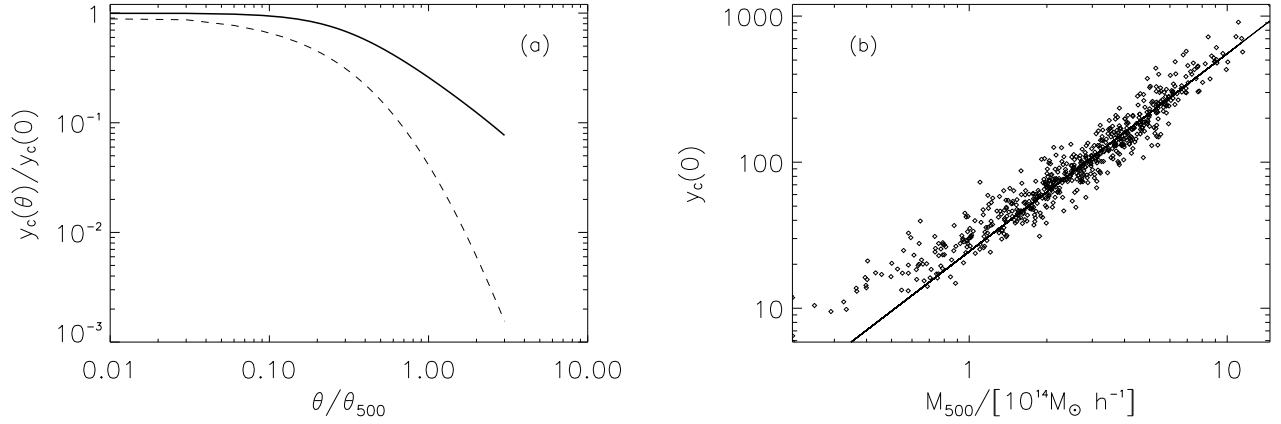


FIG. 3.— (a) Pressure profile integrated along the line of sight of a cluster with $z = 0.094$, of $M_{500} = 2.4 \times 10^{14} h^{-1} M_\odot$ and $R_{500} = 750 h^{-1} \text{Kpc}$ convolved with the antenna of the 44GHz map. Solid line corresponds to the $\beta = 2/3$ model and the dashed line to the universal pressure profile with the parameters of eq. 4. Angles are expressed in units of θ_{500} , the angle subtended by the radius R_{500} at the position of the cluster. (b) Central value of the Comptonization parameter for the clusters of our proprietary sample, derived using the measured X-ray information. The solid line correspond to the linear regression fit to the data.

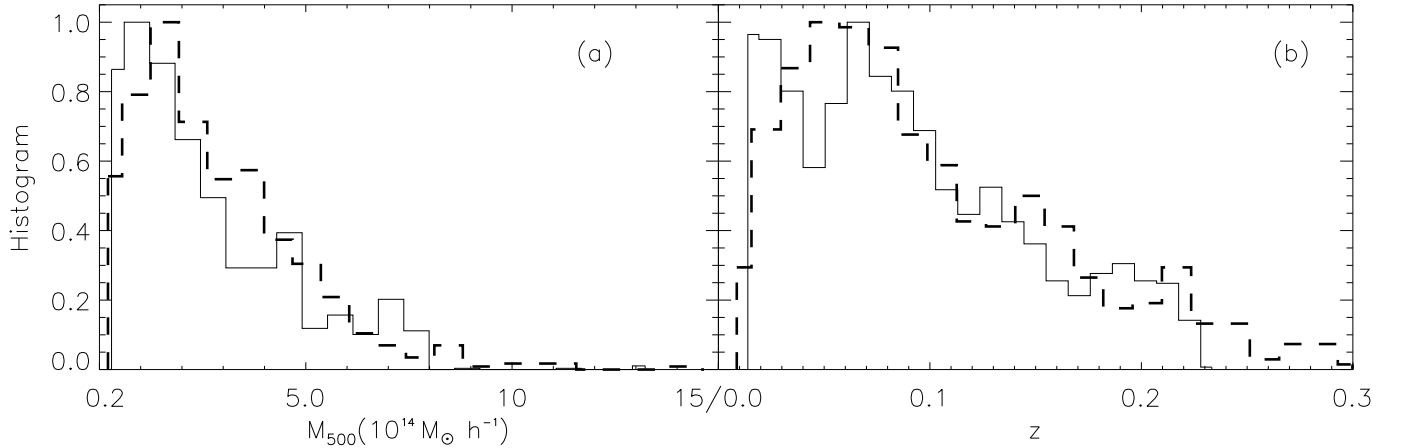


FIG. 4.— Mass (a) and redshift distribution (b) of the catalog of X-ray selected clusters (dashed line) and of clusters selected from the hydro-simulation described in Sec 3.2. For easier comparison, histograms are normalized to unity at the maximum.

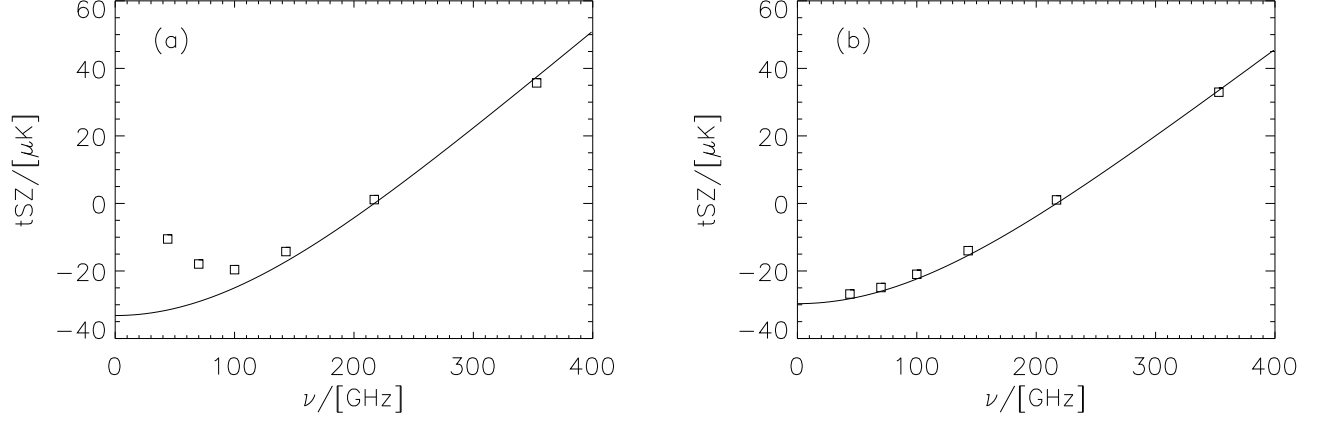


FIG. 5.— Effect of the beam dilution on the spectral dependence of the TSZ effect. Open squares represent the amplitude of the cluster TSZ effect at different frequencies, averaged over a disk of extent $2\theta_{500}$. The solid line represents the TSZ scaling $G(\nu, 0)$. Panel (a) corresponds to a cluster of mass $M_{500} = 3.64 \times 10^{14} h^{-1} M_{\odot}$ at redshift $z = 0.218$, that subtends an angle $\theta_{500} = 9.4'$. Panel (b) corresponds to $M_{500} = 7.7 \times 10^{14} h^{-1} M_{\odot}$ located at redshift $z = 0.058$, subtending an angle $\theta_{500} = 42'$.

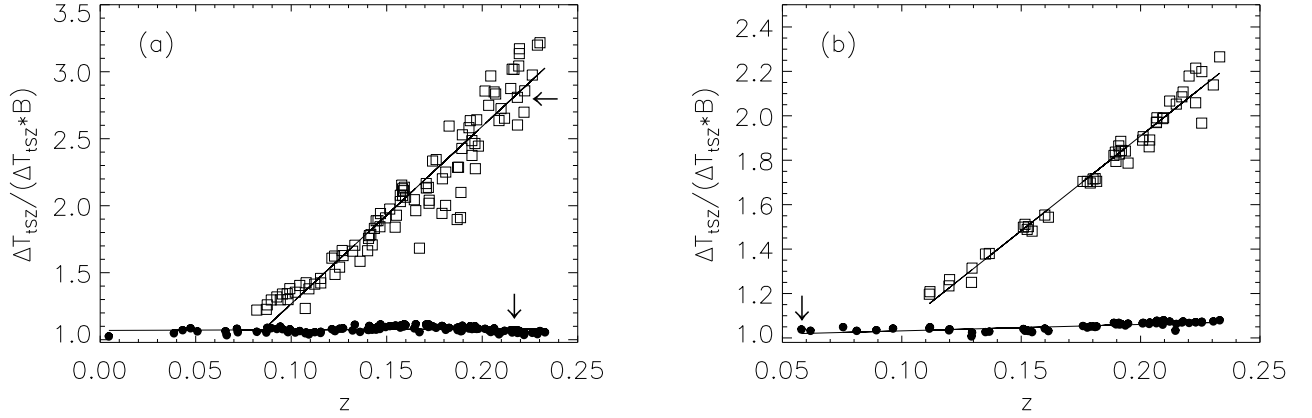


FIG. 6.— (a) Deconvolution factor for clusters in the mass range $M_{500} = 5 - 6 \times 10^{14} h^{-1} M_{\odot}$ and (b) for clusters with $M_{500} \geq 1 \times 10^{15} h^{-1} M_{\odot}$. Solid black circles represent the deconvolution factor for the 353GHz channel and open squares for the 44GHz channel. All clusters are resolved at 353 GHz but, for simplicity, at 44GHz only the fraction of unresolved clusters is shown. Arrows indicate the deconvolution factor of the clusters of Fig. 5.

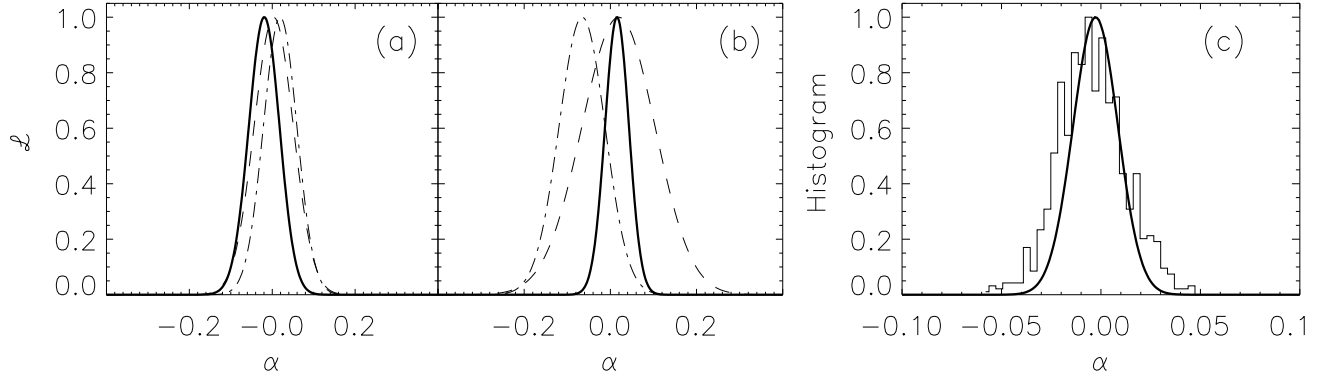


FIG. 7.— Ratio method with simulation A. Likelihood function for subsamples of 623 clusters distributed (a) in three redshift bins $z = ([< 0.11], [0.11 - 0.17], [> 0.17])$ of equal number of clusters and (b) in three mass bins $M_{500} = ([< 1.9], [0.190.37], [\geq 3.7]) \times 10^{14} h^{-1} M_{\odot}$ also with the same number of clusters. In both plots, dashed, dot-dashed and solid lines correspond to low, intermediate and high redshift/mass bins. (c) Histograms of the value of α derived from 1,000 simulations, arbitrarily normalized to unity. The smooth solid line represents a Gaussian fit to the data.

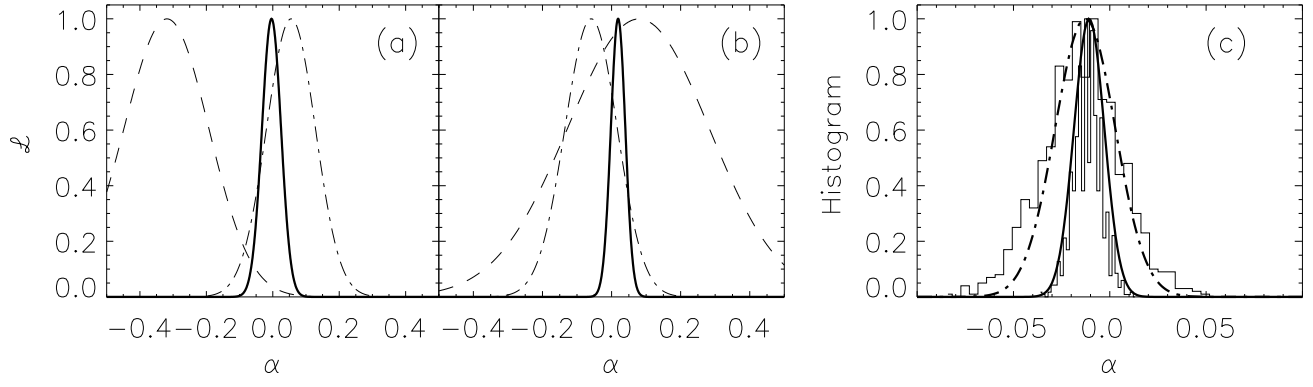


FIG. 8.— Frequency Fit method with simulation B. The cluster template was constructed using the universal pressure profile of eq. 3, with the parameters given in eq. 4. (a) Likelihoods for three different frequencies: 44GHz (dashed), 100 GHz (solid) and 343GHz (dot-dashed line) and (b) for three mass bins: dashed, dot-dashed and solid lines correspond to the mass intervals $M_{500} = ([\leq 1.9], [0.190.37], [\geq 3.7]) \times 10^{14} h^{-1} M_{\odot}$. (c) Histograms of the value of α derived from 1,000 simulations, arbitrarily normalized to unity. The dot-dashed and solid lines correspond to the gaussian fits to the histograms of y-maps constructed with the universal and $\beta = 2/3$ profiles, respectively.